



Originally published as:

Wang, Y., Pan, M., Mayanna, S., Schleicher, A. M., Spangenberg, E., Schicks, J. (2020): Reservoir formation damage during hydrate dissociation in sand-clay sediment from Qilian Mountain permafrost, China. - Applied Energy, 263, 114619.

<https://doi.org/10.1016/j.apenergy.2020.114619>

Reservoir Formation Damage during Hydrate Dissociation in Sand-Clay Sediment from Qilian Mountain Permafrost, China

Yi Wang^{1,a,b,c,d,*}, Mengdi Pan^{1,b,e}, Sathish Mayanna^b, Anja M. Schleicher^b, Erik Spangenberg^b, Judith M. Schicks^{b,*}

^a Key Laboratory of Gas Hydrate, Guangzhou Institute of Energy Conversion, Chinese Academy of Sciences, Guangzhou 510640, P. R. China.,

^b GFZ German Research Centre for Geosciences, Telegrafenberg, 14473 Potsdam, Germany

^c Guangzhou Center for Gas Hydrate Research, Chinese Academy of Sciences, Guangzhou 510640, P. R. China.,

^d Guangdong Province Key Laboratory of New and Renewable Energy Research and Development, Guangzhou 510640, P. R. China.,

^e Department for Earth and Environmental Sciences, University of Potsdam, 14476 Potsdam, Germany

Abstract

Permeability is known as a key factor affecting the gas production effectiveness from the natural gas hydrate-bearing reservoir. We studied the permeability behavior of natural clayey sand core samples from a natural hydrate-bearing reservoir in the Qilian Mountain permafrost before and after hydrate formation, as well as after hydrate decomposition. We found a substantially lower permeability after hydrate decomposition and assumed a formation damage process involving fines mobilization, migration and deposition at pore throats. The assumption was proved by SEM analysis of the filter paper separating the sample and the end caps containing the fluid ports. The analysis showed fines trapped in the paper from the outlet side. Fines migration and resulting formation damage is known from enhanced oil recovery by low salinity water flooding, but was unexpected for hydrate decomposition. The underlying mechanism was identified by a series of different permeability tests. The results indicate that fresh water released from the hydrate dissociation causes the fines

* Corresponding author. Tel: +86-20-87048054; fax: +86-20-87034664.

E-mail address: wangyi@ms.giec.ac.cn (Y. Wang); schick@gfz-potsdam.de (J. Schicks)

¹ These authors contributed equally to this work.

The short version of the paper was presented at ICAE2019, Aug 12-15, Västerås, Sweden. This paper is a substantial extension of the short version of the conference paper.

mobilization, migration and redeposition at pore throats leading to the observed permeability decrease. Obviously the large volume of released methane gas displaces the remaining saline water and separates it from the fresh water released from the hydrate. The fresh water in contact with parts of the grain framework causes the detachment of clay particles by increased electrostatic forces and clay swelling, if swellable clays are present. This is an important mechanism that has to be taken into account in the planning of gas production from low-permeability clayey hydrate-bearing formations.

Keywords: *Gas Hydrate; Reservoir Formation Damage; Qilian Mountain; Hydrate Dissociation; Gas Production*

1. Introduction

Gas hydrates are ice-like crystalline solids formed from gas and water molecules at low temperatures and elevated pressures [1]. They have therefore been found in the sediments along the continental margins as well as in permafrost regions and in locations with similar conditions. Even though only a small proportion of natural gas from natural gas hydrate reservoirs is recoverable, it is still considered as a promising clean energy resource for the future and worth exploiting. Natural hydrate deposits can be classified in 3 classes in terms of geological characteristics and reservoir conditions [2,3]. Class 1 hydrate deposits contain a hydrate interval with high hydrate saturation in the pore space and an underlying two-phase fluid zone with free gas. It is the most desirable class for exploiting since the local pressure and temperature conditions are quite close to the hydrate equilibrium [2,4]. Class 2 deposits comprise a hydrate-bearing zone overlying a mobile water zone without any free gas phase. Class 3 deposits feature only one single hydrate zone with an absence of the underlying mobile fluids zone.

Thermal stimulation, depressurization, inhibitor injection and $\text{CH}_4\text{-CO}_2$ exchange are the four most commonly proposed and used techniques in gas hydrate exploiting for both field trials and lab experiments [2,4–8]. In field trials, it is also widely agreed that a combination of these techniques may enhance the effectiveness of gas production. The field test at Mallik site in 2002 has been conducted applying thermal stimulation [9]. Other field tests such as the Mount Elbert well in Alaska North Slope in 2007 [10], as well as Mallik sites in 2007-2008 [11,12] were done by applying depressurization. In 2011, field trials in Qilian Mountain permafrost were implemented using depressurization combining with hot air and hot steam stimulation [13]. In 2012, Conoco Phillips, DOE

and JOMEC conducted a field production test, also known as the Ignik Sikumi gas hydrate field trial, by injecting a CO₂-N₂ gas mixture as a first step and depressurization as a second step [14]. With the exploration of two horizontal butted wells in 2016, a gas hydrate production test was again operated in Qilian Mountain permafrost for 23 days, yielding 1078m³ gases in total which indicated a significant increase in the production of gas compared to the single-well production test [13,15]. The above mentioned tests are all onshore field tests since they were carried out in the permafrost areas. In 2013, the first marine gas hydrate field production test was conducted in Nankai Trough in Margin of the Daini Atsumi Knoll by depressurization [16]. In 2017, China also conducted the first production tests of offshore natural gas hydrate by applying the formation fluid extraction method for 60 days [17]. It is noted from the above production trials that production values increased progressively over the tests.

Despite the fact that sand production and sediments deformation are the key factors to prevent long term gas production from hydrate bearing sediments and became an important issue during production in the field trials, experimental data are lacking or insufficient [18].

Nevertheless, for an efficient production a high permeability is of primary importance. Permeability controls fluid migration through sedimentary systems and plays also an important role in heat and chemical transfer occurring via fluid migration [19]. In hydrate-bearing sediments, permeability determines the accumulation and distribution of dissolved gas, free gas and hydrates [20]. It also affects the ability and efficiency to produce methane gas from hydrate reservoirs [21–23]. Gas and water production at longer time scales may be hindered by formation damage caused by the low permeability of the hydrate reservoir and the fresh water release from hydrate decomposition. The fresh water release may cause clay swelling and clay detachment as well-known from enhanced oil recovery by low-salinity water flooding[24–26]. At a longer time-scale of production from a hydrate-bearing reservoir formation damage may become an important issue. Among all the factors leading to different types of formation damage, the migration of fine particles is often considered as a major cause. Fine particles may physically break away during hydrodynamic flows and may accumulate in pores and thus reduce the permeability [27–29].

In this study, we investigate the changes of permeability during hydrate formation and dissociation in core samples from Qilian Mountain Permafrost and discuss the potential reasons for the observations. Hydrate reservoir in this region is a typical Class 3 hydrate deposit with an absence of the underlying mobile fluids zone. The overlying and underlying strata are sand-clay sediments with low permeability. Hence, our work may indicate the interaction between low permeability samples and production effectiveness of this kind of hydrate reservoir.

2. Experimental

2.1 Samples

The discovery of gas hydrate in Qilian Mountain permafrost is the first time to recover hydrate samples in the global low-middle latitude permafrost zone. In the Qilian Mountain permafrost 25 scientific wells have been drilled since 2008. Gas hydrate samples have been recovered from 10 of these wells below permafrost in the range of 124-396 m, while the others were found to have a series of hydrate-related anomalies [30]. In 2016, a gas hydrate trial-production project has also been carried out successfully in the Muli basin. The main well SK-0 was buttressed with two horizontal docking wells SK-1 and SK-2. Gas hydrates in Qilian Mountain are generally preserved in the Jiangcang Formation of Middle Jurassic age. The fracture-filling gas hydrates are the main reservoir type and manifest as thin layers, flakes or blocks on the fractured surface of siltstone, mudstone, and oil shale [31]. The pore-filling hydrates occur in the pores of sandstone and are difficult to observe with the naked eye [32,33]. Previous studies have shown that the Qilian gas hydrate system is an epigenetic hydrocarbon reservoir that is mainly controlled by a gaseous source, which exists in permafrost conditions, and contains a system of faults over a deep potential hydrocarbon reservoir. In addition, it has a shallower depth, thinner permafrost, and a more complex gas composition compared to the well-documented Arctic hydrate reservoirs [34].

The rock samples used in this study are originated from borehole DK-8 and SK-2 (**Fig. 1**), which are both drilling sites that recovered gas hydrate samples in northern Muli coalfield. They are gray-black muddy siltstone (DK-8-I) and fine-grained sandstone (SK-2-I, II, III) and their details are listed in Table 1. Five distinct hydrate-bearing intervals were detected in the DK-8 profile during drilling and sampling at depths of 147.8-155.9

m, 171.6-175.0 m, 226.3-236.5 m, 265.9-291.2 m and 301.8-304.2 m and three gas hydrate-bearing intervals in SK-2 at depths of 178.0-199.0 m, 250.0-262.0 m and 350.5-354.7 m respectively. In other words, the rock samples are all retrieved from the layers beneath the hydrate-bearing intervals. Drilling results also indicates that fracture-filling and pore-filling hydrates both occur in these two cores.

2.2 Characterization Methods

2.2.1 Mercury Intrusion Porosimetry (MIP)

MIP was applied for measurement of pore size distribution, pore volume and specific pore surface of the samples (Porosimeter 2000 WS, Macropore 120, Porotec). With a maximum pressure of 200 MPa the pore sizes can be measured from 3.7 to 7500 nm and the range can be extended to 120 μm using the Macropore 120 option. The results of the MIP measurement are shown in **Fig. 2**.

2.2.2 Scanning Electron Microscopy (SEM)

Sediment particles were placed on the SEM stub by adhesion with carbon tape. Samples were coated with Au-Pd at 20 mA for 120 s using BAL-TEC MED 020 to avoid charging effects during imaging. SEM images were obtained using a secondary electron detector and a backscattered electron detector in a Zeiss Ultra Plus Field Emission-Scanning Electron Microscope (FE-SEM) in a high vacuum mode and cryo mode at acceleration voltages between 10 to 20 kV with 60 μm aperture size and between 1.5 to 3 kV with 10 to 20 μm aperture size, respectively. Elemental analysis of the samples were performed at 20 kV with 120 μm aperture size in point and shoot option using a Thermo Scientific Ultra Dry Energy Dispersive Spectrometry (EDS) detector. The results of the SEM measurements are shown in **Fig. 3**.

2.2.3 X-ray diffraction analysis (XRD)

Samples were powdered in an agate mortar and mounted onto the sample holders in random orientation. XRD patterns were collected using a PANalytical Empyrean powder diffractometer with $\text{CuK}\alpha$ radiation, automatic divergent and antiscatter slits and a PIXcel^{3D} detector. The diffraction data were recorded from 5 to 85 $^{\circ}2\theta$ via a continuous scan with a step size of 0.013 and a scan time of 60 s per step. The generator settings were 40 kV and 40 mA. The characterization of the minerals in the powdered samples was done with the program “EVA” (by Bruker), and the open-source program

“Profex” was used to quantitatively assess the proportion of the mineral phases [35]. Because of the very high amount of quartz in both samples, the error in the quantitative analysis is relatively high with 3-5 %. The results are shown in **Fig. 4** and **Table 2**.

2.3 Experimental Setup for permeability measurements

As shown in **Fig. 5**, a system for experimental petrophysics (SEPP) was applied for sediment permeability measurements and hydrate formation/decomposition. SEPP consists of an autoclave with a heating/cooling jacket containing the sample setup. The inner diameter is 70 mm, and the usable length of the vessel is 250 mm. It is designed for a maximum pressure of 80 MPa. The sample setup is mounted at the top closure of the autoclave containing the feedthroughs for confining pressure oil, pore fluid inlet and pore fluid outlet, and the signal lines. The sample is separated from the confining pressure oil by means of a Viton jacket and the Hastelloy end caps. To control the sample temperature, a Pt100 temperature sensor is attached to the Viton jacket. The fluid feedthroughs in the end caps allow for pumping the pore fluid through the sample, to apply a certain pore pressure or to exchange the pore fluid. To simulate in situ pressure and temperature conditions, the autoclave is connected to a syringe pump (ISCO 100DM) to build-up the confining pressure and to a thermostat (Huber K6 s-CC-NR) to temper the sample. A detailed description of SEPP is provided elsewhere [36].

2.4 Experimental Procedures

Firstly, a dry sample was set to the desired confining pressure (6 MPa). A HPLC pump (Knauer Smartline 100) was applied to saturate the initially evacuated sample with a degassed 5% KCl solution. The temperature at the sample surface was monitored using the Pt100 RTD. The heat generated by hydrate or ice formation dissipates over the sample surface, and the ambient temperature was controlled by the thermostat to be constant at 274 K.

The permeability was estimated using Darcy’s law. For the initial experiments without hydrate, the degassed 5 % KCl solution, used to saturate the sample was pumped through the setup with rates of 0.5 ml/min, 1 ml/min, 2 ml/min, 3 ml/min, 4 ml/min, 3 ml/min, 2 ml/min, 1 ml/min, and 0.5 ml/min. For each injection rate, the injection duration was about 5 minutes. The outlet was connected to fluid sampling container open to air. The pressure on the inlet and the solution injection rate were recorded in real time.

For hydrate formation, the methane gas was injected into the sample to displace a part of pore water. Afterwards, the outlet of the setup was closed, and the sample was pressurized to 5 MPa and kept constant for methane hydrate formation. The ambient temperature was set to 274 K. After one week, the free water in pores was transformed into methane hydrate. The methane pressure was lowered but kept slightly above hydrate stability (3 MPa). The valve to the methane cylinder was closed and the connection to the piston pressure storage was opened. The pressure storage contained the same KCl solution, which is now reinjected into the sample by increasing the pressure on the backside of the piston to 5 MPa using the pressure regulator of the methane cylinder. The pressure was kept at 5 MPa for some days for the formation of hydrate with the injected water.

For the permeability measurement of the sample with hydrate, the injected solution was precooled to 274 K and injected into the sample to avoid hydrate decomposition by thermal stimulation. The outlet was connected to the pressure storage which was kept at 5 MPa. The inlet pressure and the injection rate were recorded in real time.

For hydrate dissociation, the pressure storage on outlet was removed, and the outlet was connected to the atmosphere. Afterwards, the outlet was opened to release methane gas. The volume of released methane was measured by water displacement method. Until pore pressure in the sediment reduced to the atmospheric pressure and no methane was released, the hydrate dissociation process can be considered as completed. The hydrate saturation before dissociation can be calculated as follows:

$$S_H = \frac{V_g M_H}{v_g \rho_H V_{pore}} \quad (1)$$

in which S_H represents the hydrate saturations. The gas molar volume, v_g , (mL/mol) is $2.24 \cdot 10^4$ mL/mol in this work. V_{pore} stands for the total pore volume of the sediments assuming they are incompressible and are considered constant; M_H represents the molar mass methane hydrate; and ρ_H is the densities of hydrate, which is 0.94 g/cm³ in this work.

3. Results and Discussions

3.1 Properties of the sample matrix

In this paper, the core samples from SK-2 were used for the analysis of the properties of the sediment matrix. Before permeability measurements, the samples were analyzed

for particle sizes, pore sizes and mineral components. The results from MIP showed that the pore sizes ranged from 0.1-10 μm , and particles sizes ranged from 0.01 -30 μm . The pore size of 0.7 μm obtained the highest relative pore volume, and the particle size of 1 μm obtained the highest relative percentage on sample volume. Therefore, the sample was predominantly composed of clay and silty sand. We also obtained results from EDS analysis which indicate that the main mineral components of the sample from SK-2 were quartz, carbonate, and kaolinite. Meanwhile, the boundary of different components could obviously be found from **Fig. 3**

Two samples from SK-2 were also grinded into homogeneous powders of less than 63 μm for quantitative XRD measurements. During the preparation process, the powders were surprisingly found floating on the water surface instead of dissolving into the water even after stirring. The results from XRD indicated that the main mineral component in both SK-2-I and II was quartz, with 76.5 wt% and 81 wt% respectively. Furthermore, SK-2-I contains 10 wt% feldspar, 6.5 wt% mica, 5 wt% kaolinite, and 2 wt% ankerite/siderite, whereas SK-2-II contains 7 wt% plagioclase, 4.5 wt% mica, 5 wt% kaolinite and 2 wt% ankerite/siderite (**Table 2, Fig.4**).

3.2 Reservoir formation damage by hydrate dissociation

Figure 6 shows the change of the inlet pressure during the initial permeability measurement by brine injection with different injection rates of the sample DK-8-I. Since the outlet is open to air, the inlet pressure measured with a relative pressure sensor, can be considered as the pressure difference of the inlet and outlet. As seen from this figure, the pressure difference is proportional to the injection rate. According to Darcy's law, the permeability can be calculated by the following equation:

$$K = \frac{q\eta L}{A(P_1 - P_2)} \quad (2)$$

in which, K is the effective permeability; q is the injection rate; η is the viscosity of the solution; L is the length of the sample; A is the sectional area of the sample; P_1 is the inlet pressure; P_2 is the outlet pressure.

The permeability can be calculated using Eq. 2 with the experimental results of the pressure difference shown in **Fig. 6**. The results of the calculated permeability are presented in **Fig. 7**. However, it turned out that the permeability estimates at the lower

injection rates (0.5 ml/min, 1 ml/min) were unstable. It may be due to the fact that the pump was not accurate at lower injection rates. Therefore, the calculated results with injection rate from 2 ml/min to 4 ml/min are selected for permeability estimation. The average of these permeability values is considered the effective permeability for this sample in this test. The initial permeability of the sample DK-8-I is 26.2 mD. As also can be seen from Fig. 7, the permeability of sediment slightly increases after the first injection with a rate of 3 ml/min. It may be due to the fact that the fluid dynamic leads to the particles migration in the porous media.

After methane hydrate was synthesized in the sample DK-8-I with the hydrate saturation of 33% the permeability was determined to be 15.3 mD (**Fig. 8**). The reduction of permeability is due to the fact that the methane hydrate occupies a part of the pore volume, which originally contributed to the transport network in the sample. This observation was already reported in the past [37–39]. However, in these previous studies, the permeability was recovered after hydrate dissociation in the sediment. In contrast, we observed a decrease of the permeability of sample after hydrate decomposition to 2 mD. The phenomenon can be considered as “reservoir formation damage”, which is a generic term referring to the impairment of the permeability of petroleum-bearing formations by various adverse processes. In order to determine the reason for the formation damage after hydrate dissociation, 6 experimental tests were designed. Test 1 was the initial permeability measurement. Test 2 was the permeability measurement after long time brine injection, which was applied for investigating the influence of water flow on the permeability of the sample. Test 3 was the permeability measurement after gas injection, which was applied for investigating the influence of gas flow on the permeability of the sample. Test 4 was the permeability measurement after ice formation and melting, which was similar to those of the methane hydrate. The main difference between ice melting and hydrate decomposition was the release of gas. For ice formation, the samples were firstly soaked in pure water to ensure the pores fulfilled with water, and then the temperature of the soaked sample was decreased to -15 °C for ice formation. Thus, the ice saturation in sample was nearly 100%. Afterwards, the temperature was recovered to 25 °C for ice melting. Test 5 was the permeability measurement after alternating pure water and brine water injection, which was applied for investigating the influence of the pure

water on the permeability. During Test 5, brine water was firstly injected into the sample with the injection rate of 1 ml/min for 5 minutes, and then pure water injected into the sample with the same injection rate for 5 minutes. Test 6 was the permeability measurement after hydrate formation and dissociation. Because each sample could only be damaged once, one sample could not finish all of the tests. The experimental procedures for each sample were shown in **Table 3**. The experimental results were shown in **Figs. 9-11**.

As shown in **Fig. 9**, after injection of a 5% KCl solution for 24 hours (Test 2), the permeability remained at the initial value of 37 mD. After ice formation and melting (Test 4), the permeability decreased to 27 mD. However, after hydrate formation and decomposition (Test 6, hydrate saturation = 38%), the permeability decreased to 4 mD. The experimental results indicated that the water flow dynamic might not be the reason for reservoir formation damage after hydrate dissociation. As shown in **Fig. 10**, after gas injection (Test 3), the permeability of SK-2-II increased from 91 mD to 121 mD. This result indicated that the gas fluid dynamic may also not be the reason for reservoir formation damage. After ice formation and melting (Test 4), the permeability decreased to 60 mD. After Test 6, the permeability decreased to 54 mD. It should be noted, that during the hydrate formation and dissociation test for sample SK-2-II the hydrate saturation was only 5%, which was much lower compared to that in Test 6 for sample SK-2-I. This may be the reason for the lower decrease in permeability after Test 6 in sample SK-2-II. As shown in **Fig. 11**, after ice formation and melting (Test 4), the permeability of the sample SK-2-III decreased from 32 mD to 24 mD. After alternating pure water and brine water injection (Test 5), the formation damage progressed and the permeability declined to 2 mD. The main reason for the formation damage after hydrate decomposition seems to be the fresh water released from hydrate dissociation. However, test 5 (alternating pure water and brine water injection) also leads to an obvious decrease in permeability. More work should be done to define the relationship of alternating pure water and brine water injection with permeability variety. By summarizing the experimental results from **Figs. 9-11**, three conclusions can be drawn for the investigated rock material: (1) Fluid dynamic is not the main reason for the decrease of permeability. (2) Permeability decrease by hydrate dissociation is related to hydrate saturation – high

hydrate saturations result in the release of larger amounts of water and thus stronger decrease of permeability. (3) Fresh water release from hydrate dissociation induces formation damage: The fresh water released from hydrate dissociation will increase the thickness of the electrical double layer (EDL) at the fluid-mineral interface, because there are less ions available in the pore water to compensate the surface charges at the mineral surface (e.g. [40]). The extension of the EDL increases the distant effect of repulsive forces especially for small particles like clays with a high surface to volume ratio. This might lead to the separation of clay particles sticking together or at the surface of larger particles and allows them to float in the pore water. These small particles can migrate through the pore network and may get trapped at small pore throats, decreasing or finally blocking the flow through these pores and, therefore, leading to formation damage and low permeabilities. The theoretical analysis for the reservoir formation damage after hydrate decomposition will be investigated detailed in the section 3.3.

3.3 Detection of the fine migration using SEM

In order to find the evidence for the fine migration during the formation damage process, an unused filter paper was attached on the outlet-side of the sample SK-2-I before the experimental test. The sample was cleaned by ultrasonic cleaners before experiment to avoid free particles on the sample. Thereafter, we analyzed the initial filter paper and the filter paper used during the test with SEM. The microscopic images measured by the SEM are compared in **Fig. 12**. Fine particles with different sizes could be found on the filter paper, which indicates that the fine migration has happened during the formation damage process. Elemental analysis of the particles indicates that not only quartz but also other minerals (such as plagioclase, mica, carbonate, kaolinite etc.) are involved in the fine migration to the surface of the filter paper (See **Fig. 13**).

3.4 Theoretical analysis for the reservoir formation damage

Permeability decrease in the clay-sand sediments due to the change of the injection salinity has been reported in the research of petroleum reservoir engineering for a long time. When the salinity of the solution is lower than the critical salt concentration, clay particles will disperse and migrate causing the block of pore throats [41,42]. There are many different reasons for this phenomenon like cation exchange and swelling [43]. Since we do not have expandable clay minerals like bentonite or montmorillonite, swelling is

not the explanation in our experiments. However, the release of fresh water during hydrate decomposition already causes an increase of the double layer thickness and therefore an increase of repulsion forces between small particles that can release some of these particles from the rock formation. Fluid dynamic of the fresh water will cause the migration of the fine particles resulting in permeability damage.

4. Conclusion

The permeability study on sand-clay core samples from the Qilian Mountain Permafrost revealed that fines mobilization and migration which occurred during hydrate decomposition is leading to a significant permeability decrease. This is to our knowledge the first time that formation damage by fines migration during hydrate decomposition was reported. From the results of our experiments we draw the following conclusions:

(1) The observed fines mobilization and migration is a result of the freshwater release during hydrate decomposition and the fact that the simultaneous release of a large methane volume displaced the saline pore water and separates it from the produced freshwater. In our experiments the pore pressure was lowered to atmospheric pressure during hydrate decomposition which results in a maximal volume expansion of about 200l methane per liter produced water. This effectively displaces the original saline pore water and prevents mixing of the saline and freshwater.

(2) The methane gas to water volume ratio during production depends on initial pore fluid pressure (depth) and the pressure drop required starting hydrate decomposition. As lower the required pressure drop and as deeper the reservoir is, as lower is the methane gas to water ratio during production. In deep hydrate-bearing reservoirs close to hydrate stability the produced gas volume might not sufficiently displace the original saline pore water and separate it from the produced fresh water. This could suppress the oboe described formation damage mechanism.

(3) However, as higher the hydrate saturation is, as lower is the amount of residual saline pore water that could mix with the freshwater during hydrate decomposition. This means, as higher the hydrate saturation and shallower the hydrate-bearing reservoir is, as more important the described reservoir damage mechanism in clayey sand reservoirs might become during production.

Even though our experimental sample came from the hydrate reservoir in Qilian

Mountain permafrost, we were more concerned about the observed phenomenon during our experiment rather than the sample or this specific hydrate reservoir. The conclusions were based on the experimental results but at the same time with in-depth analysis of the underlying mechanism. So a basic understanding of the above described formation damage scenario is an important prerequisite for the assessment of the economic risk prior to the gas production from clay-bearing hydrate reservoirs in a world-wide perspective.

Acknowledgments

This work is supported by National Natural Science Foundation of China (51676190), Pearl River S&T Nova Program of Guangzhou (201610010164), International S&T Cooperation Program of China (2015DFA61790), Science and Technology Apparatus Development Program of the Chinese Academy of Sciences (YZ201619), Frontier Sciences Key Research Program of the Chinese Academy of Sciences (QYZDJ-SSW-JSC033), National Key Research and Development Plan of China (2016YFC0304002, 2017YFC0307306), Youth Science and Technology Innovation Talent of Guangdong (2016TQ03Z862), Natural Science Foundation of Guangdong (2017A030313313), and also financial support from the program of China Scholarship Council (No. 201704910817) which are gratefully acknowledged.

References

- [1] Sloan ED, Koh CA. Clathrate hydrates of natural gases. 3rd ed. Boca Raton: Crc Press; 2008.
- [2] Moridis G, Collett TS, Boswell R, Kurihara M, Reagan MT, Koh CA, et al. Toward Production From Gas Hydrates: Current status, Assessment of Resources, and Simulation-Based Evaluation of Technology and Potential. SPE Reserv Eval Eng 2009;12.
- [3] Moridis GJ. Toward production from gas hydrates: current status, assessment of resources, and simulation-based evaluation of technology and potential. Lawrence Berkeley Natl Lab 2008.
- [4] Moridis GJ, Kowalsky MB, Pruess K, Lawrence Berkeley Nat L. Depressurization-

- Induced Gas Production From Class 1 Hydrate Deposits. Soc Pet Eng 2007;10:458–81.
- [5] Koh D-Y, Kang H, Lee J-WJJY, Park Y, Kim S-J, Lee J-WJJY, et al. Energy-efficient natural gas hydrate production using gas exchange. Appl Energy 2016;162:114–30.
- [6] Li S, Zheng R, Xu X, Chen Y. Dissociation of Methane Hydrate by Hot Brine. Pet Sci Technol 2015;33:671–7.
- [7] Schicks JM, Spangenberg E, Giese R, MLuzi-Helbin M, Priegnitz M, Beeskow-Strauch B, et al. A counter-current heat-exchange reactor for the thermal stimulation of hydrate-bearing sediments. Energies 2013;6:3002–16.
- [8] Wang DY, Ma XJ, Qiao J. Impact Factors of Natural Gas Hydrate Dissociation by Depressurization: A review. Explor Process Miner Resour 2014;868:564–7.
- [9] Hancock S, Collett TS, Dallimore S, Satoh A, Inoue T, Huenges E, et al. Overview of thermal-stimulation production-test results for the JAPEx/JNOC/GSC etc. Mallik 5L-38 gas hydrate production research well 2005. Bull Surv Canada 2005;585.
- [10] Hunter RB, Collett TS, Boswell R, Anderson BJ, Digert SA, Pospisil G, et al. Mount Elbert Gas Hydrate Stratigraphic Test Well, Alaska North Slope: Overview of scientific and technical program. Mar Pet Geol 2011;28:295–310.
- [11] Collett TS, Bahk JJ, Frye M, Goldberg DS, Husebo J, Koh CA, et al. Historical methane hydrate project review . Washington D.C.: 2013.
- [12] Kurihara M, Sato A, Funatsu K, Ouchi H, Yamamoto K, Numasawa M, et al. Analysis of production data for 2007/2008 mallik gas hydrate production tests in Canada. Soc Pet Eng Oil Gas Conf Exhib China 2010:2908–31.
- [13] Zhang YQ, Li XYMYM, Li XYMYM, Wang ZG. Technical Process of Gas Hydrate Production in Permafrost and Research on Oceanic Gas Hydrate Production. Explor Eng (Rock Soil Drill Tunneling) 2016;43:154–9.
- [14] Boswell R, Schoderbek D, Collett TS, Ohtsuki S, White M, Anderson BJ. The Ignik Sikumi field experiment, Alaska North Slope: Design, operations, and implications for CO₂-CH₄ exchange in gas hydrate reservoirs. Energy and Fuels 2017;31:140–53.
- [15] Zhu YH. Land field gas hydrate resources exploration and trial production obtains a series

of achievements. News Lett China Geol Surv 2017;3:1–5.

- [16] JOGMEC. Gas produced from methane hydrate (provisional). vol. In JOGMEC. 2013.
- [17] Li J, Ye J, Qin X, Qiu H, Wu N, Lu H, et al. The first offshore natural gas hydrate production test in South China Sea. China Geol 2018;1:5–16.
- [18] Konno Y, Fujii T, Sato A, Akamine K, Naiki M, Masuda Y, et al. Key Findings of the World's First Offshore Methane Hydrate Production Test off the Coast of Japan: Toward Future Commercial Production. Energy & Fuels 2017;31:2607–16.
- [19] Waite WF, Santamarina JC, Cortes DD, Dugan B, Espinoza DN, Germaine J, et al. Physical properties of hydrate-bearing sediments. Rev Geophys 2009;47:RG4003.
- [20] Nimblett J, Ruppel C. Permeability evolution during the formation of gas hydrates in marine sediments. J Geophys Res 2003;108:2420.
- [21] Delli ML, Grozic JH. Experimental determination of permeability of porous media in the presence of gas hydrates. J Pet Sci Eng 2014;120:1–9.
- [22] Moridis GJ. Numerical studies of gas production from methane hydrates. SPE Gas Technol. Symp., Society of Petroleum Engineers; 2003.
- [23] Moridis GJ, Collett TS, Dallimore SR, Satoh T, Hancock S, Weatherill B. Numerical studies of gas production from several CH₄ hydrate zones at the Mallik site, Mackenzie Delta, Canada. J Pet Sci Eng 2004;43:219–38.
- [24] Song W, Kovscek AR. Direct visualization of pore-scale fines migration and formation damage during low-salinity waterflooding. J Nat Gas Sci Eng 2016.
- [25] Hussain F, Zeinijahromi A, Bedrikovetsky P, Badalyan A, Carageorgos T, Cinar Y. Enhanced oil recovery through low salinity fines-assisted waterflooding: Laboratory and mathematical modelling. Soc. Pet. Eng. - SPE Asia Pacific Oil Gas Conf. Exhib. APOGCE 2014 - Chang. Game Oppor. Challenges Solut., 2014.
- [26] Zeinijahromi A, Al-Jassasi H, Begg S, Bedrikovetski P. Improving sweep efficiency of edge-water drive reservoirs using induced formation damage. J Pet Sci Eng 2015.
- [27] Krueger RF. An overview of formation damage and well productivity in oilfield operations. J Pet Technol 1986;38:131–52.

- [28] Wilson MJ, Wilson L, Patey I. The influence of individual clay minerals on formation damage of reservoir sandstones: a critical review with some new insights. *Clay Miner* 2014;49:147–64.
- [29] Wilson L, Wilson MJ, Green J, Patey I. The influence of clay mineralogy on formation damage in North Sea reservoir sandstones: A review with illustrative examples. *Earth-Science Rev* 2014;134:70–80.
- [30] Li B, Sun YH, Guo W, Shan XL, Wang PK, Pang SJ, et al. The mechanism and verification analysis of permafrost-associated gas hydrate formation in the Qilian Mountain, Northwest China. *Mar Pet Geol* 2017;86:787–97.
- [31] Wang PK, Zhu YH, Lu ZQ, Huang X, Pang SJ, Zhang S, et al. Geochemistry and genesis of authigenic pyrite from gas hydrate accumulation system in the Qilian Mountain permafrost, Qinghai, northwest China. *Sci China-Earth Sci* 2014;57:2217–31.
- [32] Zhu Y, Zhang Y, Wen H, Lu Z, Jia ZY, Li Y, et al. Gas Hydrates in the Qilian Mountain Permafrost, Qinghai, Northwest China. *Acta Geol Sin Ed* 2010;84:1–10.
- [33] Wang PK, Zhu YH, Lu ZQ, Guo XW, Huang X. Gas hydrate in the Qilian Mountain permafrost and its distribution characteristics. *Geol Bull China* 2011;30:1839–50.
- [34] Wang PK, Huang X, Pang SJ, Zhu YH, Lu ZQ, Zhang S, et al. Geochemical dynamics of the gas hydrate system in the Qilian Mountain Permafrost, Qinghai, Northwest China. *Mar Pet Geol* 2015;59:72–90.
- [35] Bergmann J, Friedel P, Kleeberg R. BGMN — a new fundamental parameters based Rietveld program for laboratory X-ray sources, its use in quantitative analysis and structure investigations. *Comm Powder Diffraction, Int Union Crystallogr CPD News* 1998;20:5–8.
- [36] Spangenberg E, Seyberth K, Heeschen KU, Priegnitz M, Schicks JM. A Quick Look Method to Assess the Dependencies of Rock Physical Sediment Properties on the Saturation With Pore-Filling Hydrate. *J Geophys Res Earth* 2018;123:5588–98.
- [37] Katagiri J, Konno Y, Yoneda J, Tenma N. Pore-scale modeling of flow in particle packs containing grain-coating and pore-filling hydrates: Verification of a Kozeny–Carman-based permeability reduction model. *J Nat Gas Sci Eng* 2017;45:537–51.

- [38] Li G, Wu D-M, Li X-S, Lv Q-N, Li C, Zhang Y. Experimental measurement and mathematical model of permeability with methane hydrate in quartz sands. *Appl Energy* 2017;202:282–92.
- [39] Zhao J, Fan Z, Dong H, Yang Z, Song Y. Influence of reservoir permeability on methane hydrate dissociation by depressurization. *Int J Heat Mass Transf* 2016;103:265–76.
- [40] Revil A, Darot M, Pezard PA. From surface electrical properties to spontaneous potentials in porous media. *Surv Geophys* 1996;17:331–46.
- [41] Civan F. *Reservoir Formation Damage*. USA: Gulf Professional Publishing; 2015.
- [42] Khilar KC, Fogler HS. The Existence of a Critical Salt Concentration for Particle Release. *J Colloid Interface Sci* 1984;101:215–400.
- [43] Wu ZR, Li YH, Sun X, Wu P, Zheng JN. Experimental study on the effect of methane hydrate decomposition on gas phase permeability of clayey sediments. *Appl Energy* 2018.

TABLE Captions

TABLE 1 Geological parameters of the samples from Qilian mountain permafrost

TABLE 2 Quantitative XRD analysis using the open source Rietveld Program “Profex”

TABLE 3 Arrangement of experimental tests for SK-2-I, SK-2-II, and SK-2-III

FIGURE Captions

FIGURE 1 Samples SK-2-I-III taken from one core piece recovered from borehole SK-2 in 355 m depth. The dimensions of the samples are 61.3 mm length and 24.9 mm in diameter.

FIGURE 2 Measurements of pore size distribution and particle size distribution for samples from SK-2 site by using Mercury Intrusion Porosimetry (MIP)

FIGURE 3 SEM-EDS analysis of dry sample from SK-2, Qilian mountain permafrost

FIGURE 4 XRD patterns of SK-2-I and SK-2-II used for quantitative analysis (kaol=kaolinite, qtz=quartz, fsp=feldspar)

FIGURE 5 Schematic of apparatus

FIGURE 6 Changes of pressure difference during brine injection with different injection rate

FIGURE 7 Permeability calculated by Darcy’s law during brine injection with different injection rate

FIGURE 8 Initial permeability, permeability after hydrate formation, and permeability after hydrate dissociation of sample DK-8-I

FIGURE 9 Permeability measurement results after experimental test 1, test 2, test 4, and test 6 for sample SK-2-I

FIGURE 10 Permeability measurement results after experimental test 1, test 3, test 4, and test 6 for sample SK-2-II

FIGURE 11 Permeability measurement results after experimental test 1, test 4, and test 5 for sample SK-2-III

FIGURE 12 SEM micrographs of the filter paper before and after reservoir formation damage of sample SK-2-I

FIGURE 13 Mineral component analysis of the particles on filter paper after reservoir formation damage by SEM and EDS

Table 1 Geological parameters of the samples from Qilian mountain permafrost

Sample	Borehole	Depth (m)	Length (mm)	Diameter (mm)	Porosity (%)	Sample Density (g/cm ³)	Matrix Density (g/cm ³)
DK-8-I	DK-8	387	48.8	25.0	8.2	2.41	2.62
SK-2-I	SK-2	355	60.5	24.9	4.4	2.41	2.52
SK-2-II	SK-2	355	61.4	24.8	1.7	2.46	2.50
SK-2-III	SK-2	355	61.9	25.0	2.0	2.45	2.50

Table 2 Quantitative XRD analysis using the open source Rietveld Program “Profex”

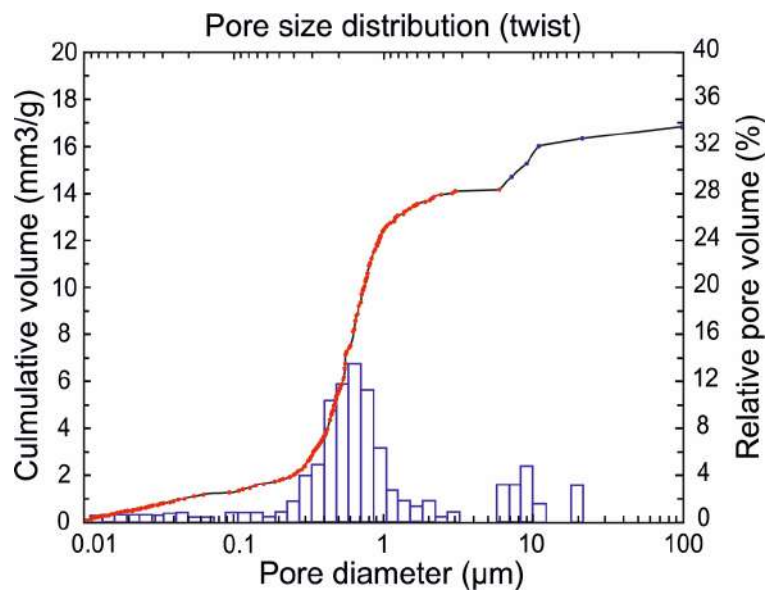
Sample	Quartz	Plagioclase	K-feldspar	Mica	Ankerite/Siderite	Kaolinite
SK-2-I	76.5%	9%	1%	6.5%	2%	5%
SK-2-II	81%	7%	n.d.	4.5%	2%	5%

Table 3 Arrangement of experimental tests for SK-2-I, SK-2-II, and SK-2-III

Sample	Test1	Test2	Test3	Test4	Test5	Test6
SK-2-I	Yes	Yes	No	Yes	No	Yes
SK-2-II	Yes	No	Yes	Yes	No	Yes
SK-2-III	Yes	No	No	Yes	Yes	No



Fig.1 Samples SK-2-I-III taken from one core piece recovered from borehole SK-2 in 355 m depth. The dimensions of the samples are 61.3 mm length and 24.9 mm in diameter.



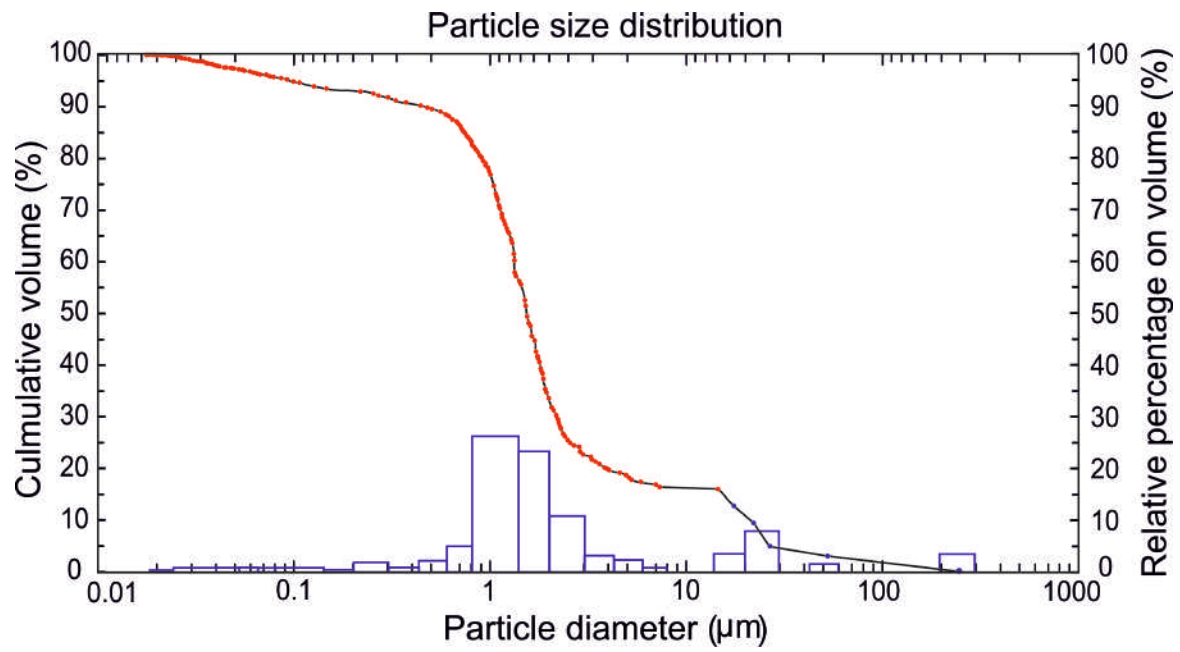


Fig.2 Measurements of pore size distribution and particle size distribution for samples from SK-2 site by using Mercury Intrusion Porosimetry (MIP)

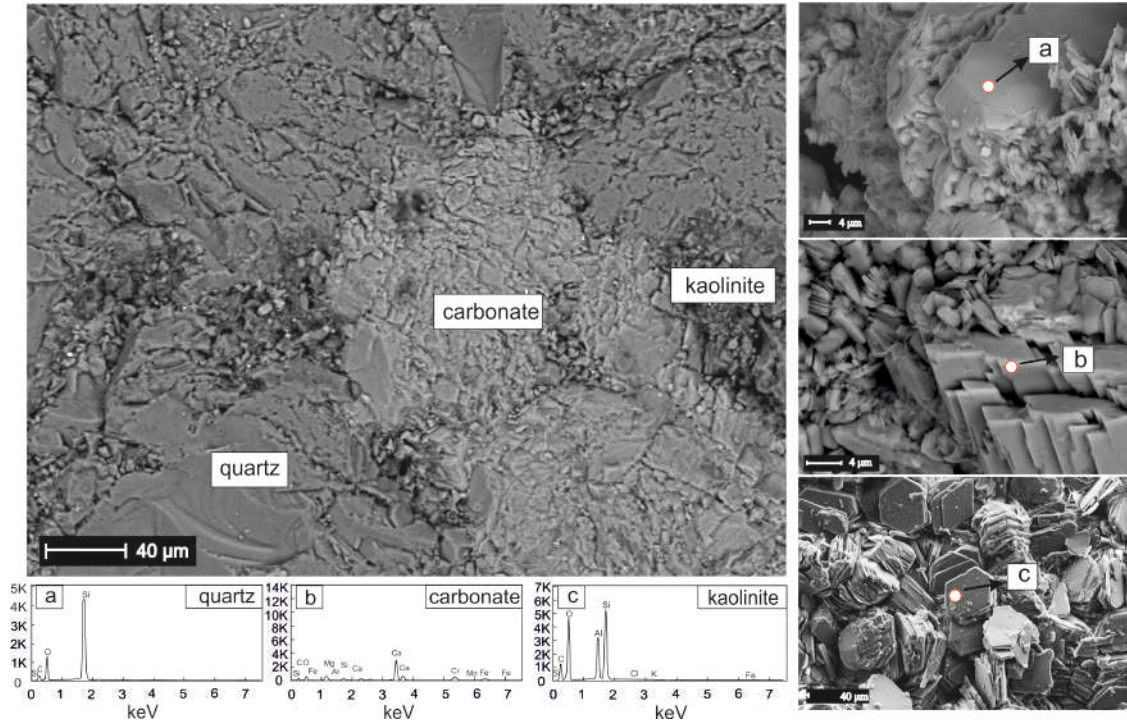


Fig. 3 SEM-EDS analysis of dry sample from SK-2, Qilian mountain permafrost

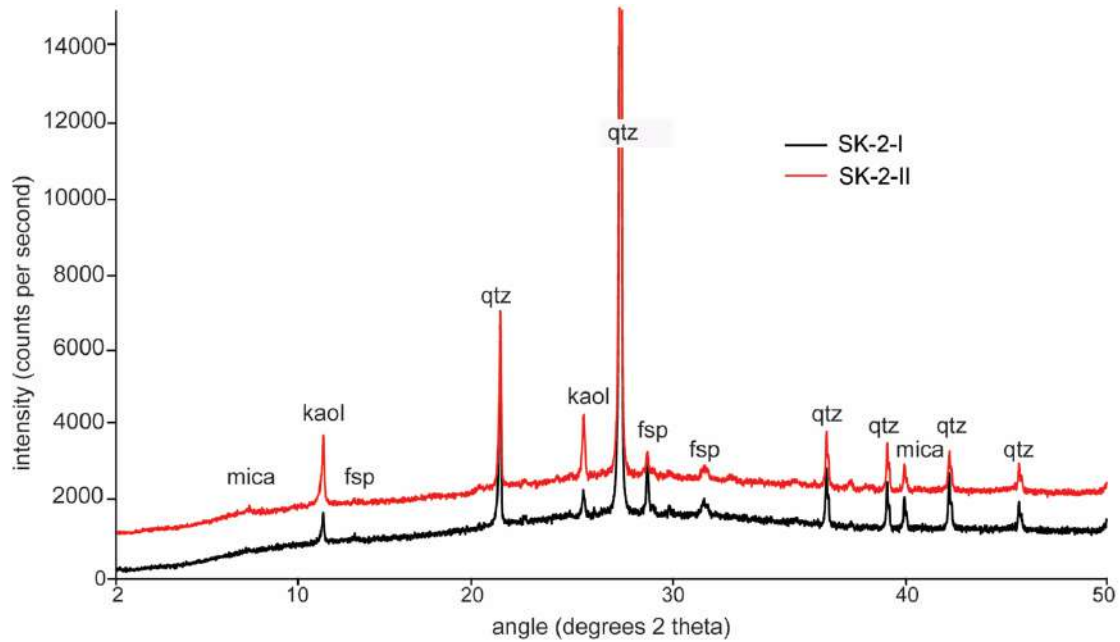


Fig. 4 XRD patterns of SK-2-I and SK-2-II used for quantitative analysis (kaol=kaolinite, qtz=quartz, fsp=feldspar)

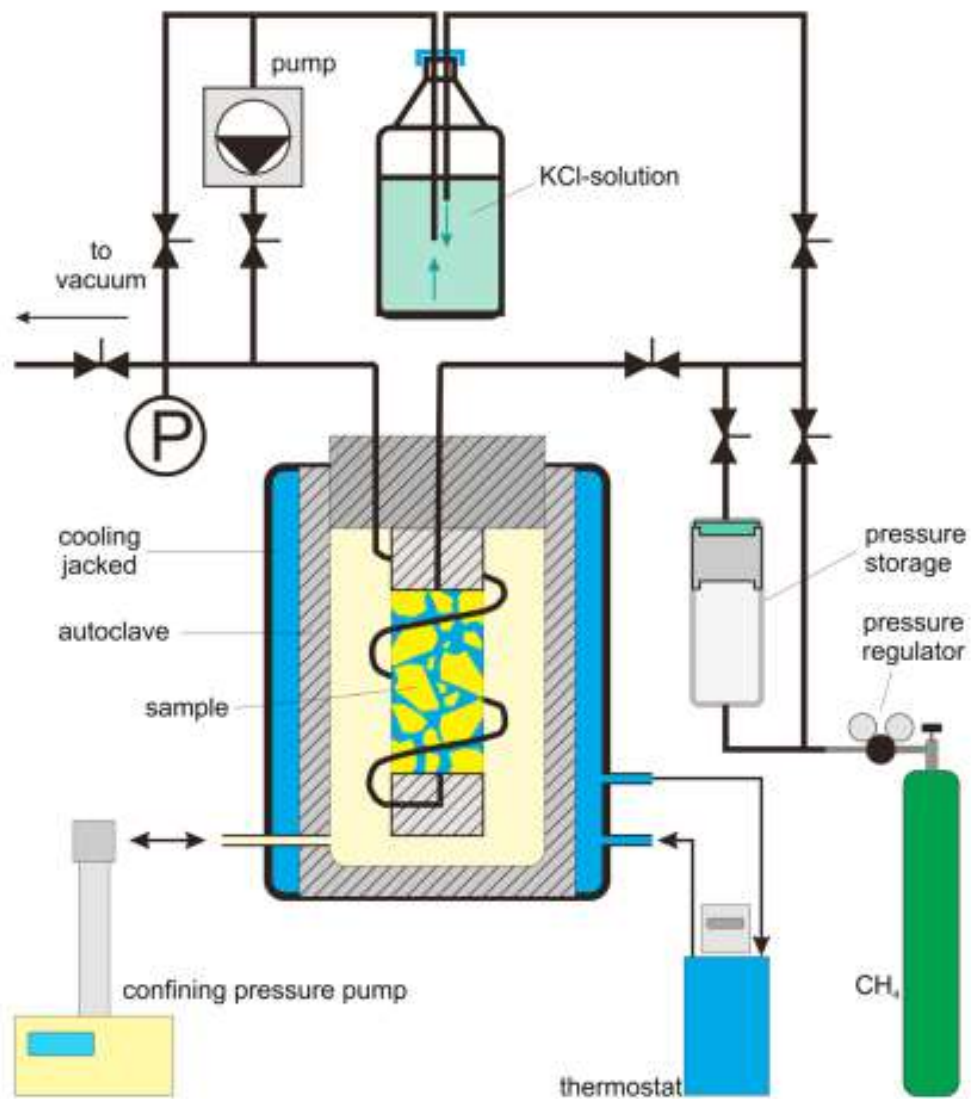


Fig. 5 Schematic of setup

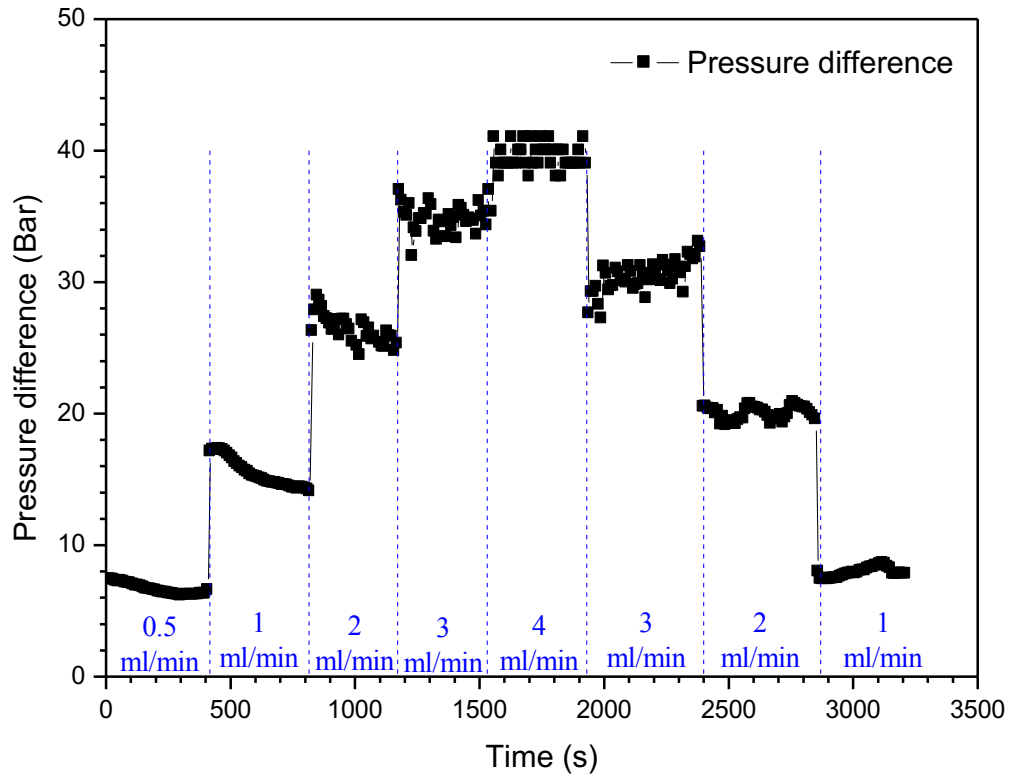


Fig. 6 Changes of pressure difference during brine injection with different injection rate

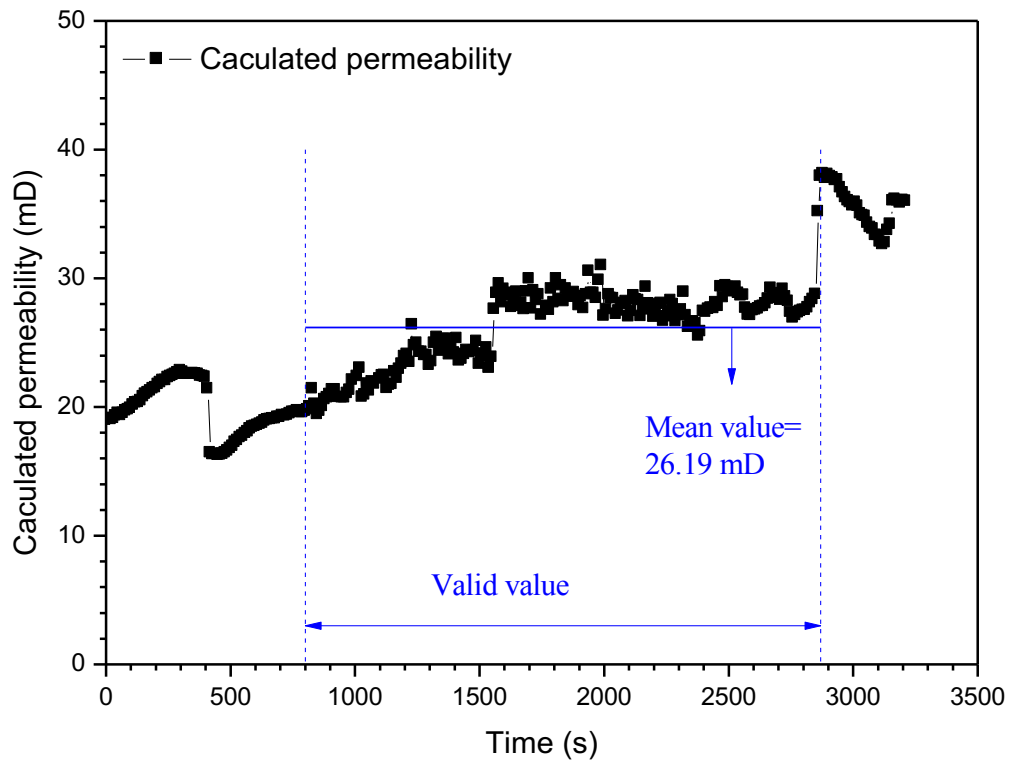


Fig. 7 Permeability calculated by Darcy's law during brine injection with different injection rate.

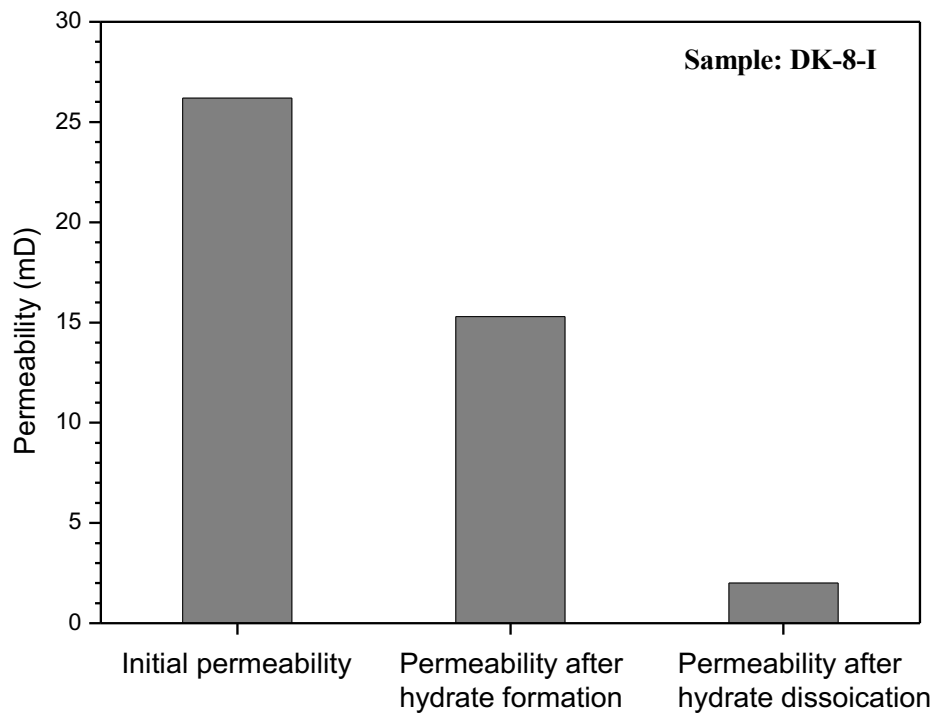


Fig. 8 Initial permeability, permeability after hydrate formation, and permeability after hydrate dissociation of sample DK-8-I

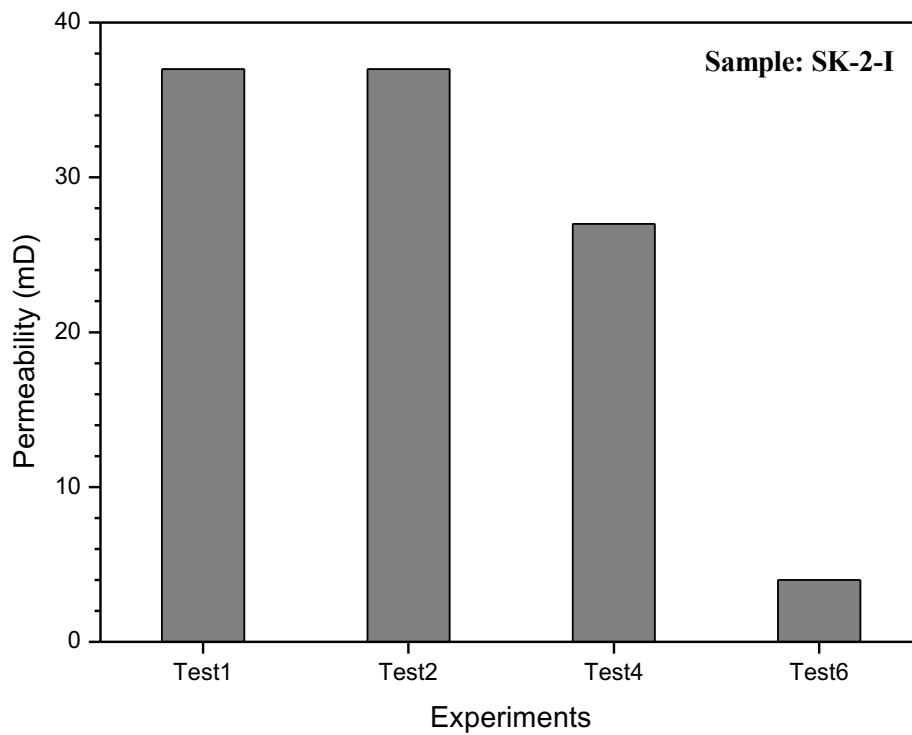


Fig. 9 Permeability measurement results after experimental test 1, test 2, test 4, and test 6 for sample SK-2-I

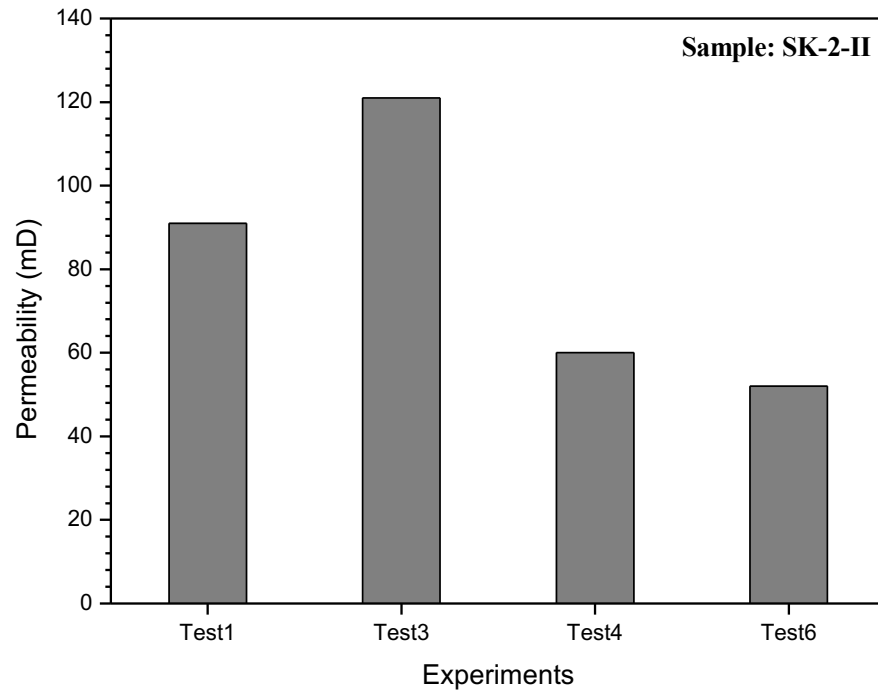


Fig. 10 Permeability measurement results after experimental test 1, test 3, test 4, and test 6 for sample SK-2-II

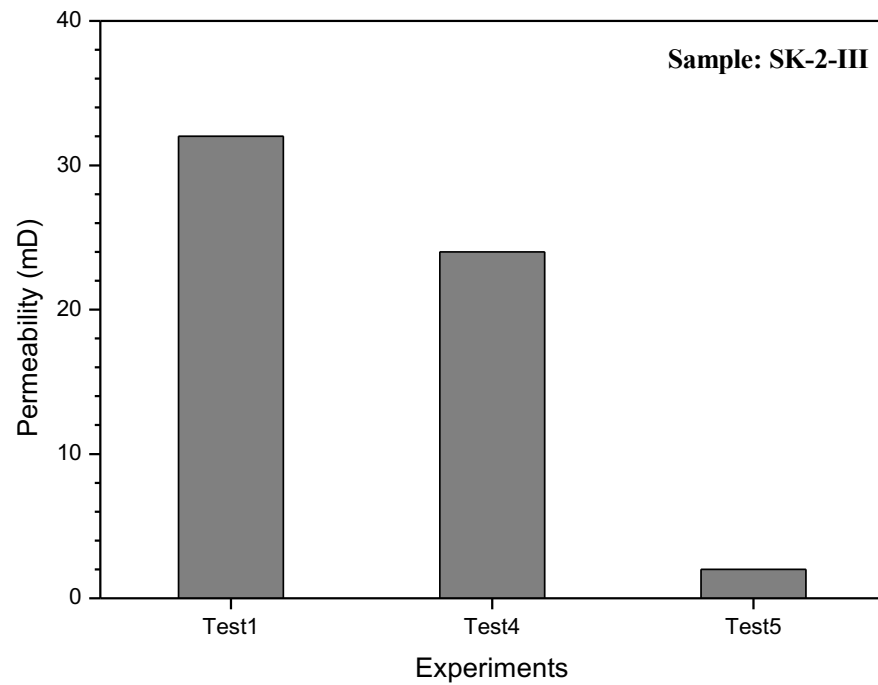


Fig. 11 Permeability measurement results after experimental test 1, test 4, and test 5 for sample SK-2-III

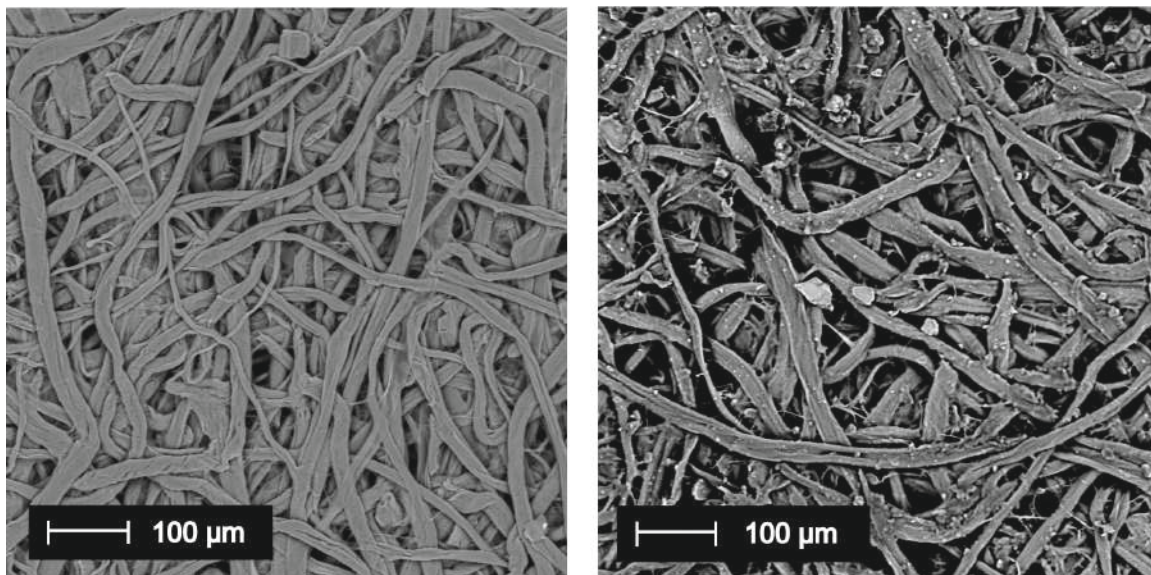


Fig. 12 SEM micrographs of the filter paper before and after reservoir formation damage of sample SK-2-I

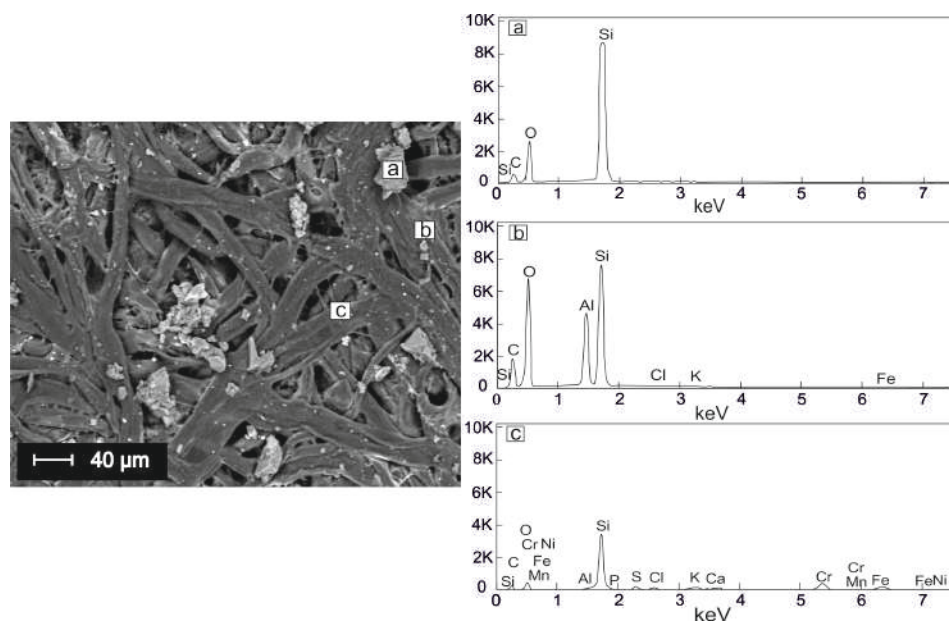


Fig. 13 Mineral component analysis of the particles on filter paper after reservoir formation damage by SEM and EDS